Rethinking Excavated-Earth Concrete: Water Transport in Sustainable Earthcretes

S. Iotti [a], L. Lanzoni [b,c,*], A.M. Tarantino [b,c], M. Viviani [a]

[a] *HEIG-VD/HES-SO - Haute Ecole d'Ingénierie et de Gestion du Canton de Vaud, Route de Cheseaux 1, CH-1401 Yverdon, Switzerland*
[b] *DIEF-Department of Engineering" Enzo Ferrari", University of Modena and Reggio Emilia, 41125 Modena, Italy*
[c] *CRICT - Centro Interdipartimentale di Ricerca e per i servizi nel settore delle Costruzioni e del Territorio, University of Modena and Reggio Emilia, 41125 Modena, Italy*
** Corresponding author:*
E-mail address: luca.lanzoni@unimo.it (L. Lanzoni)

Abstract

Durability is a critical—yet often underestimated—aspect of concrete technology and sustainable construction materials. Parameters like CO_2-eq emissions (GWP) are key indicators of a Life Cycle Assessment (LCA) and should be systematically evaluated over a structure's full-service life and its depreciation time (economic life). This ensures that economic, environmental, and societal efficiency are well-balanced. However, the length of a structure's service and economic life cycles depends on its durability and reparability. Durability is therefore a key issue for ensuring structural integrity, long-term functionality, environmental resilience, and economic sustainability. This study examines the effect on the durability of the interaction between water and Shot-Earth, an innovative earth-based concrete also applied to structural elements including reinforced walls, beams, vaults and slabs. Two structural-grade Shot-Earth mixtures were evaluated in detail. The sorption coefficients were found to be 0.8 kg/($m^2h^{0.5}$) and 3 kg/($m^2h^{0.5}$) over 24 hours, reflecting the influence of water-soil affinity, binder content, porosity, and internal cohesion. Conversely, higher stabilizer content, reduced voids, and higher density allow to reduce the coefficient to 0.2 kg/($m^2h^{0.5}$) such as for Ordinary Portland Cement (OPC) concrete in comparison. It is also shown that Shot-Earth exhibits water permeability in the range of 1.965×10^{-16} m² to 3.373×10^{-16} m², more than one order of magnitude higher than OPC concrete. The experimental findings were supported by both FE modeling and a numerical simulation, providing reliable tools to predict and optimize the durability of earth-based materials such as Shot-Earth.

Keywords: Shot-Earth, Earth-based Materials, Sustainability, Water Absorption, Durability, FE Simulation

Abbreviations: SE2, Shot-Earth 772; SE1, Shot-Earth 771; SE1-2, Shot-Earth both mixtures 771 and 772; C45, Ordinary Concrete (OPC) 45.5 MPa; IRA, Initial Rate of Absorption; FE: Finite Element

1. Introduction

Soil is one of the earliest building materials used by humanity. Formed through a long and slow physic disaggregation processes promoted by natural weathering such as freeze-to-thaw cycles, rain, wind, and manufacturing processes, soil has supported human structures since as early as 10'000 BCE in Mesopotamia (the current Iraq, **[1]**) till recent years. Noteworthy techniques such as adobe **[2,3]**, cob, waffle and daub, torchis, pisé (or beaten earth), and rammed earth remain widely used nowadays, providing shelter for an estimated 30–50% of the global population **[4]** (**Fig. 1**). These methods offer significant ecological benefits including energy efficiency, resource conservation, and positive social impact. The indoor well-being provided by earthen buildings is also a key factor that makes them a preferable choice **[5–7]**.

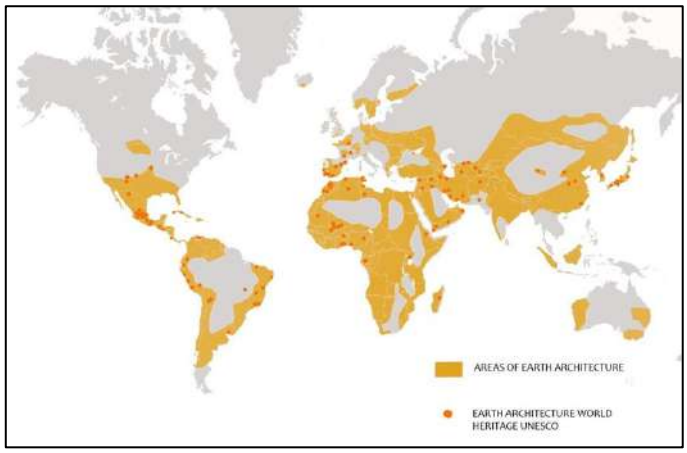

Fig. 1. World map for still-on-use earth – UNESCO Heritage

Cities such as Shibam, often referred to as the "Manhattan of the Desert" in Yemen **[8]**, are located in seismic zones and have withstood natural hazards for hundreds of years. Nevertheless, recent climate change-induced flooding has severely challenged these traditional materials and revealed a critical shortage of skilled workers able to repair them. Despite these ancient solutions, the improvement in durability was considered nearly compulsory over the years by traditional builders that used natural additives such as tree resins, cow dung, animal blood, and oils from plants or animals. These substances helped make soil more water-resistant and durable, and they were low-cost and easy to provide. However, these natural stabilizers became less effective. For this reason, the modern construction industry still relies predominantly on concrete — a material associated with high environmental costs, including CO_2 emissions, landfill accumulation, and intensive energy consumption. A growing issue is the disposal of excavated soil in urban areas, which contributes to pollution, urban disruption, and logistical complications. In response to these challenges, Shot-Earth has emerged as a promising sustainable material. It combines soil, sand, and an optional amount of cement and it is applied at high

velocity to achieve dense compaction and early-stage green strength, thus eliminating the need of conventional formwork **[8–14]** (**Fig. 2a**). Notably, the cement content is reduced up to 60% as compared to that of an OPC concrete, making it an environmentally attractive alternative. Shot-Earth applications are several: the main advantage of using dry shotcrete **[15]** technology lies in the high placement speed to ensure good self-compaction. This promotes high density coupled with low permeability, thus allowing to cast rapidly important volumes of earthen materials characterized by a significant strength within the first curing stages. However, the variability of the characteristics of the excavation earth from site to site is recognized as a major challenge for any earth-based material as it can potentially affect various physical properties **[16,17]**. To overcome this drawback, the research activity also investigates the technology of pressed-earth, which involves small cylindrical samples which are tested to predict straightforwardly the engineering properties of Shot-Earth by means of suitable correlations **[11]**. Such a technology, combined with Shot-Earth, was also used to experimentally evaluate long-term viscoelastic behavior of earthen composites **[18]**. Shot-Earth can thus be concerned to the manufacture of walls, slabs (**Fig. 2b**), beams, shells, domes, vaults **[19]**, and other structural members for both repairs and rehabilitations, as for reinforcement and replacing failed materials, as well as for surfaces protection, even for geotechnical applications such as slope stabilization. Summarily, it can be either employed in such situations in where other solutions, such as pressed-earth instead, would require operational difficulties just as filling cavities, and walls behind pipes or other similar hurdles.

Fig. 2. (a) Shot-Earth projection leaned 45° over the horizontal direction (from **[9]),** (b) Test of a Shot-Earth slab

Despite Shot-Earth's potential, its long-term durability has not been comprehensively studied, especially in relation to water exposure, as well as for other earthen materials. Indeed, recent studies have shown that moisture content strongly influences both the water absorption and the mechanical strength in clayey and earthen materials, showing a considerable drop in performance as the water uptake increases **[20–23]**.

Durability **[24]** refers to the ability of a material or structure to retain its functionality and serviceability over time when exposed to environmental stressors. For soil-based materials, whether stabilized or not, water is typically the most harmful agent, leading to surface erosion, infiltration, and degradation during extreme events such as floods. Additionally, other atmospheric factors—such as wind **[25]**, frost **[20,26]**, solar radiation **[27]**, fire **[28]**, and chemical agents **[24,29,30]** — especially when acting simultaneously, may significantly compromise the physical and mechanical performances of earth-based materials and structures **[31,32]**. Knowledge of durability also guides contractors' material choices and supports national strategies for achieving carbon neutrality by 2040–2050. An emblematic example is Nsutam in Ghana, where an entire village was wiped away during a flood in 1970 **[33]**. It has been one of the most detrimental examples of vulnerability of earthen structures by water-contact. Therefore, this study aims to:

1. evaluate Shot-Earth under capillary rise, immersion, and pressurized absorption conditions;
2. compare its performance with ordinary Portland cement concrete (OPC);
3. develop and validate Finite Element (FE) simulations and simplified analytical models;
4. offer practical recommendations for implementation and design.

This study is capitally important for the sustainability profile of Shot-earth. Sustainability has been defined through decades of studies, often shaped by painful lessons. The case of Thomas Midgley Jr. is a well-known reference for understanding the risks of ignoring long-term environmental impacts. He first developed tetraethyl lead (TEL), which was technologically efficient but caused widespread lead poisoning (saturnism) **[34–36]**. Later, he co-developed Freon, a chlorofluorocarbon (CFC) that became widely used in refrigeration and air conditioning. CFCs were later shown to be powerful ozone-depleting substances and, at the same time, highly potent greenhouse gases.
It is important to note that ozone depletion and climate change are two distinct phenomena:

- Ozone depletion results from the breakdown of stratospheric ozone by CFCs and related substances, which increases exposure to harmful UV radiation and is linked to higher rates of skin cancer (e.g., melanomas).
- Climate change is primarily driven by the greenhouse effect, caused by the accumulation of gases such as CO_2, CH_4, N_2O, and certain industrial gases (including CFCs).

Because different greenhouse gases have different warming effects, their emissions are expressed in terms of CO_2 equivalents (CO_2-eq) using the Global Warming Potential (GWP) metric **[37,38]**. Switzerland ratified the Paris Agreement and, since 2019, has committed to achieving net-zero CO_2 emissions by 2050. For the construction industry, a key reference is the SIA 390/1 standard **[39]**, which focuses on CO_2. This standard applies a modular life-cycle assessment (LCA) approach to buildings and

extends the boundary beyond "cradle-to-gate" to also include the end-of-life phase. It expresses impacts as a total amount of CO_2-eq per square meter and per year over the building's reference service life. This means that eco-materials must not only have a low embodied CO_2-eq content, but also demonstrate declared performance characteristics, durability, reparability, and ease of maintenance. These aspects are essential to ensure long-term sustainability and to avoid premature replacement, hidden emissions, and unnecessary resource use. Furthermore, the standard requires accounting for cases where the service life is shortened: if a building is reconstructed earlier than planned, the permitted CO_2-eq allowance must be reduced pro rata. In addition, this standard — together with broader Swiss federal policies such as the Climate and Innovation Act (LCI), the Code of Obligations' compulsory non-financial reporting, and the federal administration's model role (which includes achieving net-zero already by 2040) — requires that new construction materials demonstrate proven efficiency across economic, environmental, social, and technical dimensions. Finally, the standard strongly promotes circular economy principles. It requires defining a clear strategy for the end-of-life phase of buildings and encourages the reuse of elements. Re-employed building components can be credited with a reduction of up to 20% of the CO_2-eq impact compared to equivalent new materials. Shot-Earth has been investigated primarily as a methodology rather than as a material **[9]**. A systematic approach has been developed to prepare and optimize mixes, and structural calculation models have been studied to allow structural engineers to design elements in reinforced Shot-Earth. The projection (spraying) method has been designed to allow adjustments to the mix design during placement, without interrupting the process. This characteristic is particularly important for walls, both structural and non-structural, since the lower portion of a wall may require much lower water sensitivity than the upper portions. In conventional earth-based construction, it is common to include an OPC concrete element at the base of the wall to address this issue. Furthermore, Shot-Earth does not inherently depend on a specific binder. If a zero-CO_2 cement is developed, it can be directly applied to Shot-Earth. Additional strategies have also been studied to achieve near-zero-CO_2 Shot-Earth, even when a modest quantity of OPC cement is used, thanks to the efficiency of the dry projection process. In this respect, Shot-Earth aligns with the philosophy of the SIA 390/1 standard and, more broadly, with the net-zero objectives of Swiss federal policies. In this study, the simplest version of Shot-Earth is used. Mixes 771 and 772, which contain pure Portland cement, serve as the baseline for preparing and optimizing Shot-Earth for real applications. As an example, a recent series of tests carried out for a construction project led to the optimization of the mix design: starting from the standard 772, it was refined into a 10/4/2 mix containing a commercially available low-clinker CEM II cement, without any loss of performance. Full-scale structural element tests confirmed the robustness of the entire Shot-Earth methodology — from mix design to production

process, structural calculation, and detailing — and were validated through large-scale tests on wood–Shot-Earth composite beams (**Fig. 3**).

Fig. 3. Example of a Shot-Earth and timber coupling: (a) Shot-Earth projection in wooden formwork to realize 9 m length beams, (b) surface flattening, and (c) Shot-Earth consolidation

2. Materials and Methods

2.1. Materials

Three materials were investigated in this study: Shot-Earth 772 (SE2), Shot-Earth 771 (SE1), and ordinary Portland cement concrete (C45). The Shot-Earth mixes were dry blends of excavated soil, coarse sand (0–8 mm), and Portland cement (CEM I 42.5N), with weight proportions of 7/7/2 and 7/7/1, respectively. Water was not added to the dry mix directly, but it has been introduced at the nozzle at 3% by volume during projection. The soil used in the present study contained less than 25% of clay and lime and over 50% of sand and gravel, in compliance with requirements reported in previous studies **[9–11]**. Several specimens, including cubes, cylinders, and slabs, were fabricated and cured under laboratory conditions for 28 days prior to durability testing. The C45 was produced using a standard mix design of cement (340 kg/m^3), aggregates (0–4 mm: 816.9 kg/m^3; 8–16 mm: 427.9 kg/m^3; 16–32 mm: 700.2 kg/m^3), two superplasticizer additives (1.312 and 0.246 kg/m^3), and water (164 kg/m^3). Several cube specimens were tested after 28 days of curing, reaching an average compressive strength of about 45.5 MPa. Dry and apparent densities, and porosity were determined in compliance with relevant regulations **[40,41]**, whereas compressive strength was assessed in accordance to EN 12390-3:2019 **[42]**. The modulus of elasticity has been evaluated by following to EN 13412:2006 **[43]**, while Poisson's ratio has been assessed in accordance with ASTM C469/C469M-14 **[44],** see **Table 1.**

Table 1. Resuming table of materials features concerning Shot-Earth durability assessment

	Bulk density$_{dry}$ δ (kg/m^3)	Apparent density, (kg/m^3)	Compression strength, f_{cm} (MPa)	Porosity, ϕ (%)	Young module, E (MPa)	Poisson coefficient, υ
SE2	2050.58 ± 2.12	2495.95 ± 2.05	20.30 ± 1.27	17.84 ± 0.02	14923.90 ± 1989	0.2240 ± 0.16
SE1	2027.56 ± 9.98	2496.15 ± 4.06	7.72 ± 0.33	18.77 ± 0.28	6198.12 ± 418	0.1938 ± 0.06
C45	2327.98 ± 11.77	2597.53 ± 6.71	45.50 ± 3.0	10.37 ± 0.24	37485.54 ± 3974	0.2000 ± 0.03

Moreover, X-ray diffraction (XRD), X-ray fluorescence (XRF), and Scanning Electron Microscopy (SEM), and particle size analyses were employed to characterise the mineralogical and chemical composition of the Shot-Earth mixtures **[45–48]**, as these properties may strongly affect their durability. In more detail, XRD was employed to identify the mineralogical composition, which strongly influences water absorption and, in turn, the development of cementitious phases in stabilized soils. For instance, excessively high content of quartz, that is chemically inert and non-reactive with cement, does not contribute to cementation and it reduces the formation of C–S–H gel to bind the matrix. This can increase intermediate porosity, promote water penetration, and ultimately decrease the long-term durability of the material **[49].** For XRD, the analyses were conducted using a D2 Bruker SDD-160-1 detector to a compound sample. The soil was previously dried at 105°C, finely grind, homogenized, and placed into a circular holder. The results were conducted using the open-source software Profex **[45].** Moreover, to identify the oxides and other chemical elements in the compounds, providing essential information on the presence of cementing or reactive, X-ray fluorescence spectroscopy (XRF) was also performed using a Rigaku NEX DE spectrometer. As well as for XRD, the soil was oven-dried, finely grinded, and pressed by using rounded holders in groups of three to guarantee homogeneity. Lastly, Zeiss EVO Scanning Electron Microscope was deployed for SEM images combined with XRD. With the aim to quantify the most microstructural details, it was decided to perform the following scan process: one scan at 1000X regarding the matrix, one regarding the asperities or evident particularities to 1000X, and one of the latter to 2000X. In addition, a granulometric analysis and Atterberg limit tests were also conducted to assess the soil's physical and mechanical properties in compliance with EN 933-1 **[50]** and SN 670 816a **[51]**. Particle size analysis was conducted to determine the granulometric distribution by controlling packing density, compaction, and also the water retention properties.

2.2. Experimental Approach

2.2.1 Initial Rate of Absorption (IRA)

Capillary absorption was tested following BS EN 13057:2002 **[52]** and AS/NZS 4456.17:2003 **[53]**. Nine specimens were partially submerged (10 mm) in water, and mass gain was measured at fixed time intervals—5 minutes, 12 minutes, 30 minutes, 1 hour, 2 hours—in which the waterfront was recorded on each side of the samples, then 4 hours, and finally 24 hours (**Fig. 4**). Sorptivity coefficients (S) were calculated for each mix and listed in **Table 4.**

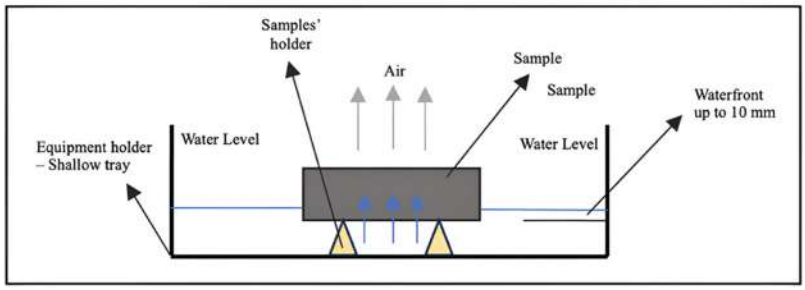

Fig. 4. Initial Rate of Absorption (IRA) test setup

2.2.2. Immersion Test

Following the IRA test, see **Fig. 5,** the same specimens underwent full immersion for up to 7 days. Mass gain and water content were recorded daily. Saturation was reached rapidly in SE1, while SE2 and C45 showed slower uptake rates.

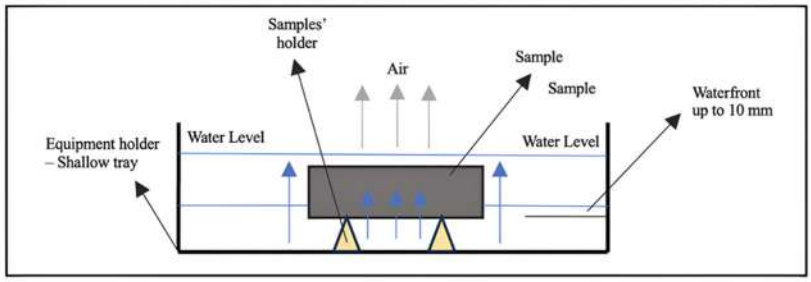

Fig. 5. Immersion test setup

2.2.3. Water Permeability Test

Water permeability tests were conducted under two pressure regimes following BS EN 12390-8 **[42]** and DIN 1048-5 **[54]**. The first attempt (500 kPa for 72h) caused rapid failure in both SE1 and SE2: the applied pressure has resulted too high to cause oversaturation of the surfaces of the cubes, thus leading to formation of surface droplets. For this reason, the first attempt was not accomplished. Consequently, a second attempt was carried out (200 kPa for 72h) and it was completed successfully. Penetration depths were measured after specimen splitting (**Fig. 6, Table 6**) by Brazilian compression test **[55]**. Thus, real intrinsic permeability and diffusivity coefficients were inferred for each material according to **[15,52,56]**.

Fig. 6. Example of visible waterfront in SE1 after pressure exposure

2.3. Analytical and FE Modeling

Although the transport of water in cementitious porous media has been widely studied, the development of reliable tools for simulating this phenomenon remains a significant challenge. This is particularly relevant when considering key transport properties such as capillary water absorption and gas permeability, which are essential for assessing the durability and mechanical performance of cement-based materials. These parameters influence how different substances move throughout the material, affecting hydration reactions, and long-term structural behavior. This dynamic process can create areas where the behavior of the material may vary unexpectedly. Models such as the *Brutsaert model* **[57],** the *Boltzmann* transformation approach **[58],** and the *Zhou model* **[59]** were developed to quantify the dependence of water absorption on the saturation level of porous materials. It is worth noticing that these models are based on empirical and theoretical basics drawn from soil mechanics, employing simplified geometries and being limited to unsaturated condition, which is unlikely to occur under real-world conditions in dealing with cementitious materials as concrete. While numerical modeling is widely available, finite element (FE) models for predictive purposes often require excessive boundary work, making the development of a feasible model more complex and time-consuming than necessary **[60]**. These challenges, along with numerous approximations, have discouraged many authors from continuing with this approach. Notwithstanding, an example of FE modeling to water absorption for capillary water-front rising for both SE1 and SE2, and C45 is given in this study. FE simulations were performed in ANSYS to model capillary water rise (**Fig. 7**). The Volume of Fluid (VOF) model was applied, and porous media behavior was approximated using Ergun's theory, later adjusted via *Darcy-Forchheimer* formulation **[57–59].** The mesh resolution was 0.5 mm, yielding 26,202 nodes and

25,600 elements. Material porosity, particle size (D_p), and calculated permeability were calibrated against experimental data. Effective particle sizes were adjusted (e.g., 0.2–0.5 cm for SE1 and SE2) based on best-fitting results (see **Section 3.7**), as listed in **Table 6**. Moreover, a simplified analytical absorption model based on *Lin Yang*'s assumptions **[61,62]** is also proposed as a polynomial relationship between degree of saturation and mass uptake based on IRA test data according to **Eq. (1)** and **Eq. (2)**:

$$\frac{S_{i=1\ldots n}(\Lambda)}{S_{i=0}} = 1 - 1.5\,\Lambda + 0.5\,\Lambda^2 \quad (1)$$

$$\Lambda = \frac{m_x - m_d}{m_s - m_d} \quad (2)$$

where $S_{i=1\ldots n}(\Lambda)/S_{i=0}$ depends on the degree of saturation, Λ, with the full-saturated mass, m_s, the full-dried mass, m_d, and the mass at any given time interval, m_x.

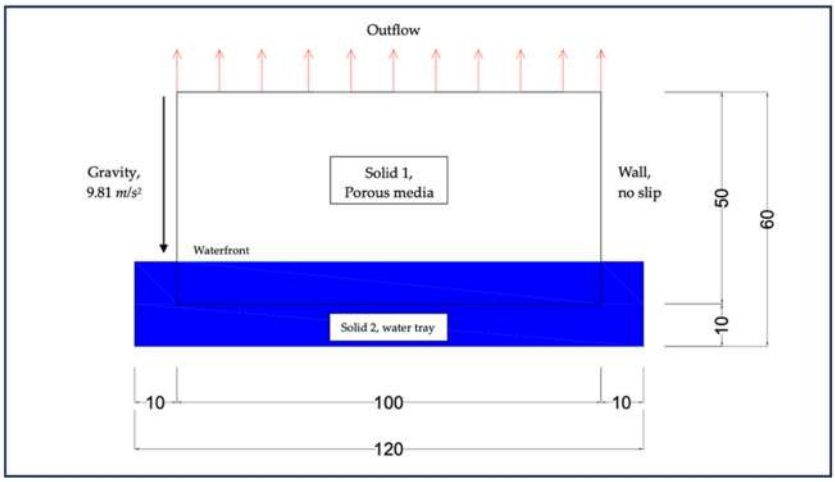

Fig. 7. Sketch of the FE model to assess the Initial Rate of Absorption; solid 1, porous media, and solid 2 filled of water

3. Results

3.1. XRD-XRF-SEM Images

The XRD's phases identification (**Fig. 8a-b**) has found a prevalence of quartz, calcite, muscovite, chamosite, albite, dolomite, chlorite, and kaolin. The high calcite content is optimal to guarantee intermolecular bonding and mechanical resistance **[46–48]**, with minimal kaolin and no organic matter. XRF measurements confirmed high contents of silica oxide (SiO_2) and calcium oxide (CaO), both critical for mechanical strength and hydration potential (**Fig. 8c-d**, **Table 2**).

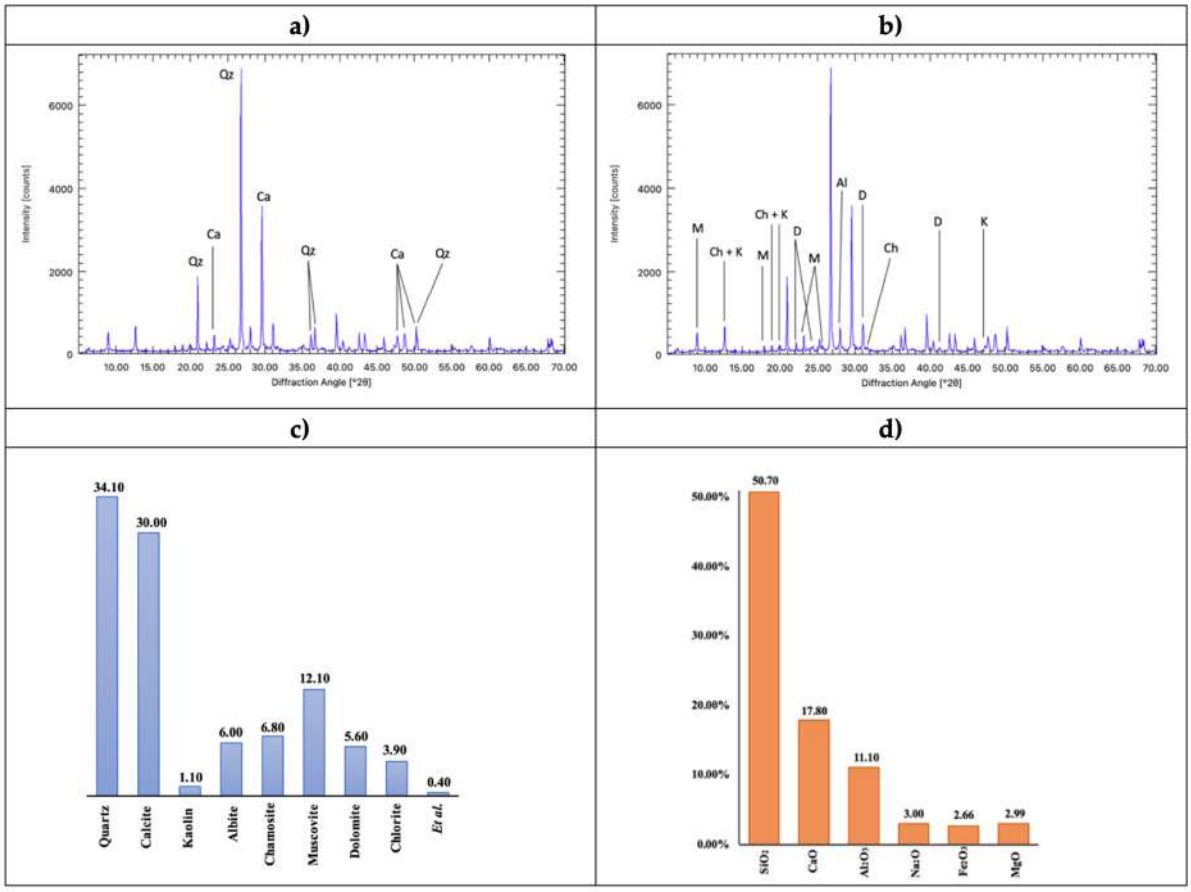

Fig. 8. (a) XRD main peaks, (b) while complementary research has delineated traces of kaolin, albite, chamosite, muscovite and gibbsite; (c) phases were found with XRD, while (d) oxides were found by XRF: all of those are expressed in %-mass

Table 2. XRF chemical elements, on percentage of total mass (wt%). Reliability of results with XRD

Elements	*O*	*Si*	*Ca*	*Al*	*Fe*	*Na*	*Mg*	*K*	*Ti*	*P*	*S*	*Sc*	*Mn*	*Cl*
% - Mass	33.33	30.99	19.63	7.31	2.95	2.66	2.19	1.4	0.37	0.19	0.324	0.078	0.07	0.04
SD	2.89	1.37	1.24	0.22	0.29	0.06	0.06	0.08	0.032	0.015	0.015	0.016	0.005	0.0033

Moreover, SEM images coupled with XRD were adopted to better understand the microstructural evolution and phase composition of the samples, allowing correlations between hydration products, porosity distribution, and surface densities. From the morphological perspective, SE2 (**Fig. 9**) and C45 (**Fig. 10**) displayed a dense and well-integrated matrix, while SE1 (**Fig. 11**) showed increased porosity and irregular bonding due to its lower cement content. For SE2 the predominance was of silicon, oxygen, and calcium. Localized concentrations of iron-calcium were also detected as white paddles ranging between 0.10–0.50 μm. According to *R.V. Balendran et al*. **[18]**, the hydration products of cement are complex and may be estimated as follows: 70% of fully hydrated cement consists of 80% calcium silicates and 20% calcium aluminates, 20% calcium hydroxide, and about 10% unhydrated cement, debris, calcium aluminate, or clinker residue **[19]**. Cement hydration up to 90 days was investigated using SEM, XRD, and EDXA techniques as proposed by *He et al.* **[63]**. XRD results showed ettringite formation during early hydration stages, which disappeared after 28 days (C-A-H). SEM analysis at later stages

confirmed that ettringite needles were no longer observed, giving way to microstructural densification as a rheological control mechanism. The C-A-H bonds contribute to microstructural densification but only marginally to mechanical strength. Their role, however, may be fundamental to regulate the absorption behavior and, in turn, to improve durability. As compared to C-A-H bonds, silicate hydration increases more slowly. During curing, filamentous structures form and progressively elongate until they intertwine and densify. These generate C-S-H bonds, which are crucial for the mechanical properties of cementitious materials, although they also leave micro-cavities unfilled. In SE2, the matrix appeared regular, homogeneous, and well-integrated with clasts and aggregates, despite the intentionally reduced cement content (estimated over 20% less). The resolution of the images did not allow a clear distinction of all hydration products **[20]**. However, calcium hydroxide was visible and identifiable by its morphology as large flat crystals irregularly grouped on the surface. These hydration products are responsible for mechanical resistance, compactness, and high density, possibly linked to the absorption capacity of Shot-Earth. This behavior might be explained by the limited amount of cement present in Shot-Earth. On contrary, no calcium–silicon hydrate spikes were identified. Conversely, SE1 showed a higher degree of surface alteration due to its leaner amount of binder within the mixture. As shown in **Fig. 9** indeed, the paste appeared more rarefied and less amalgamated, producing large intermolecular voids highlighted in the yellow frames. Shadowed spots in the images further underline this higher porosity, which had resulted crucial during the experimental campaign by creating preferential channels, thus promoting absorption. Finally, minor concentrations of zirconium (*Zr*) were detected.

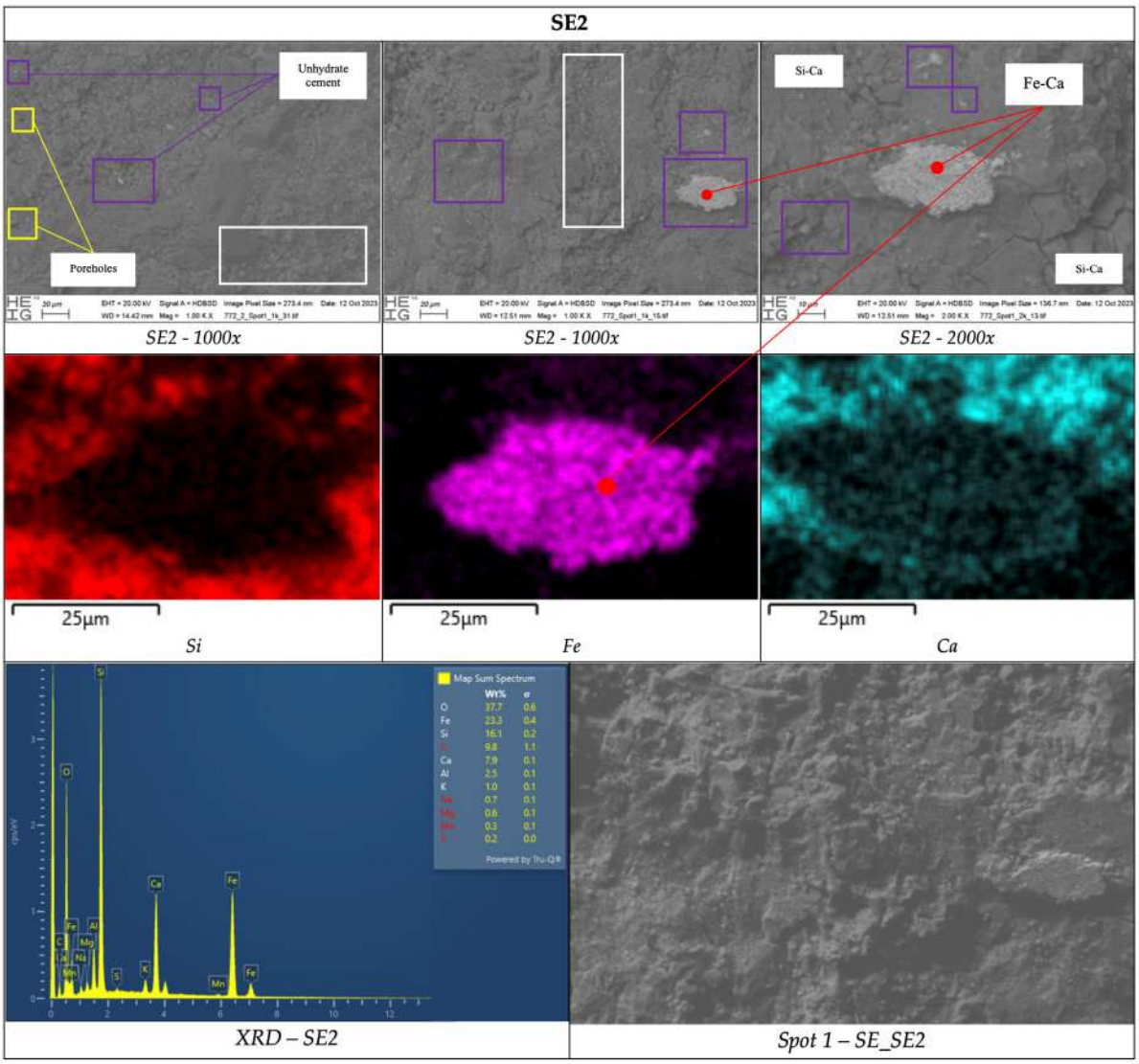

299

300 **Fig. 9.** SEM images for SE2 whom the XRD was applied on matrix, debris, and particularities

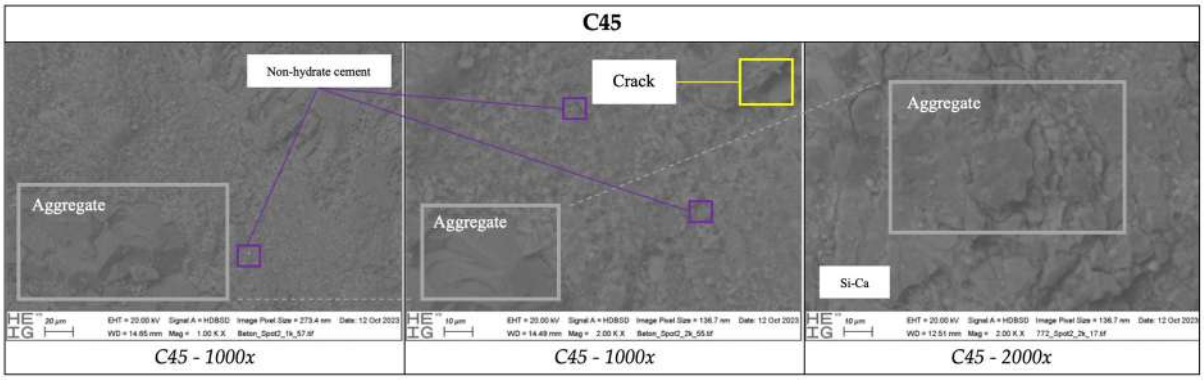

301

302 **Fig. 10.** SEM images for C45

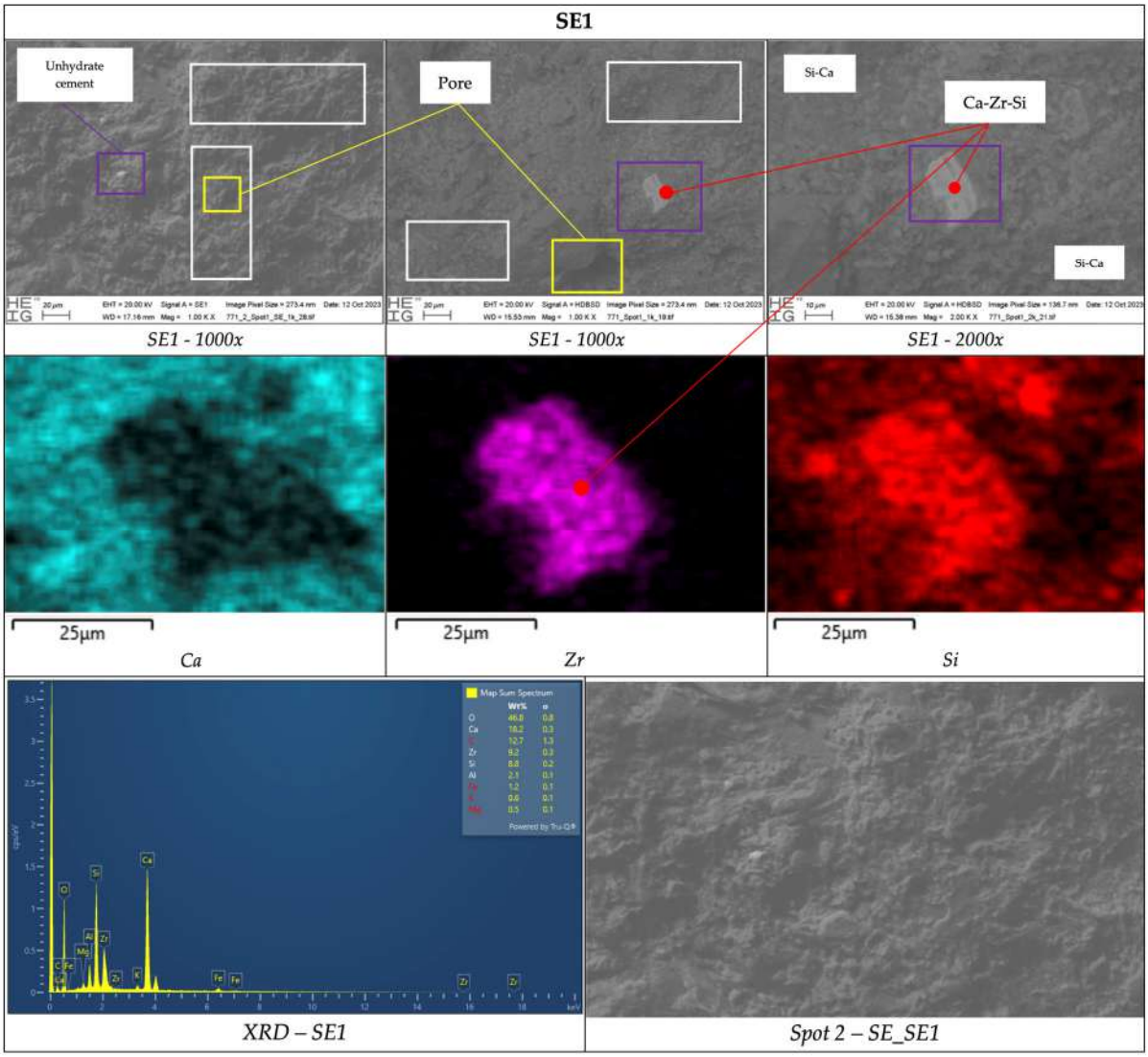

Fig. 11. SEM images for SE1 whom the XRD was applied on matrix, debris, and particularities

3.2. Soil Classification

The soil was classified as CL (Clayey Silt with sand) according to the Unified Soil Classification System (USCS), with approximately 75% of silt and clay content. Plasticity index and liquid limit are provided in **Table 3,** whereas the particle-size distribution curve is shown in **Fig. 12**. The average particle diameter, essential for subsequent modeling, was established to be 0.09 cm.

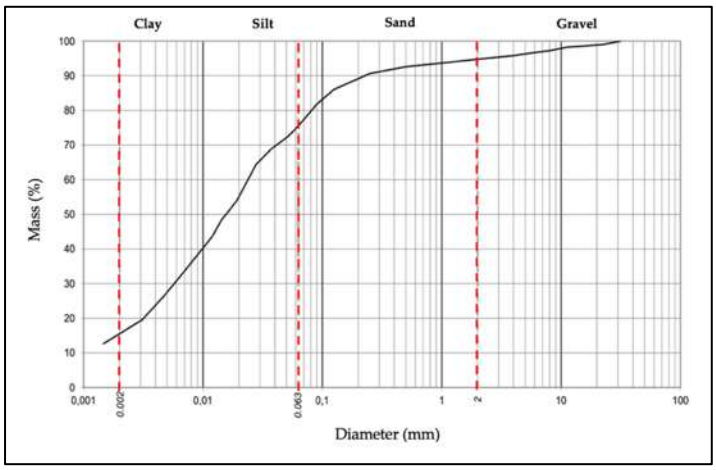

Fig. 12. Granulometric curve mass-passing sieve diameter (mm)

Table 3. Geotechnic parameters for soil used for Shot-Earth

Atterberg limits		
W_L	21.5	%
W_P	14.5	%
I_P	7.0	%
Soil percentages		
Gravel (2-63 mm)	5.2	%
Sand (0.063-2 mm)	19.3	%
Silt + Clay (<0.063 mm)	75.5	%
Silt (0.002-0.063 mm)	59.5	%
Clay <0.002 mm	16.0	%
Classification USCS	CL	-

3.3. Initial Rate of Absorption (IRA)

The IRA test evaluated the water uptake behavior of SE1, SE2, and C45 over a 24-hour period under capillary conditions. As shown in **Fig. 13**, SE1 exhibited the highest initial sorptivity, followed by SE2, while C45 displayed minimal absorption due to its low porosity and high compaction. Only SE1 reached full saturation within the 24-hour. Sorption coefficients (S_5 for the 5-minute interval and S_{24} for 24-hour) were extracted for each mixture and listed in **Table 5**. Linear capillary behavior was observed for SE1, while SE2 and C45 showed nonlinear saturation curves **[64]**. Detailed water uptake trends at various time intervals are presented within **Fig. 14a–f**. In detail, the slope-derived sorptivity profile for SE1 is shown in **Fig. 15**. After 2 hours of partial immersion, the waterfronts were recorded and approximated to the nearest 0.5 cm, finding 35 mm, 50 mm, 20 mm, respectively, for SE2, SE1, and C45.

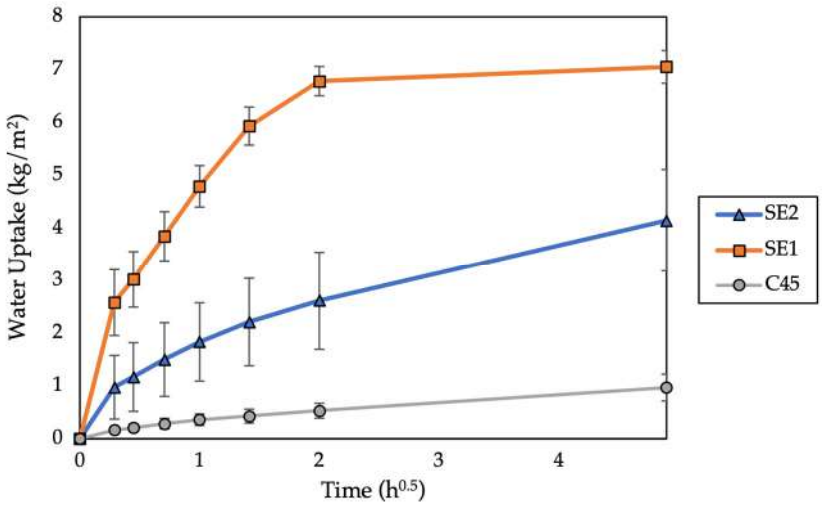

Fig. 13. Water uptake over 24 hours for SE1, SE2, and C45 during the IRA test. Standard error is provided

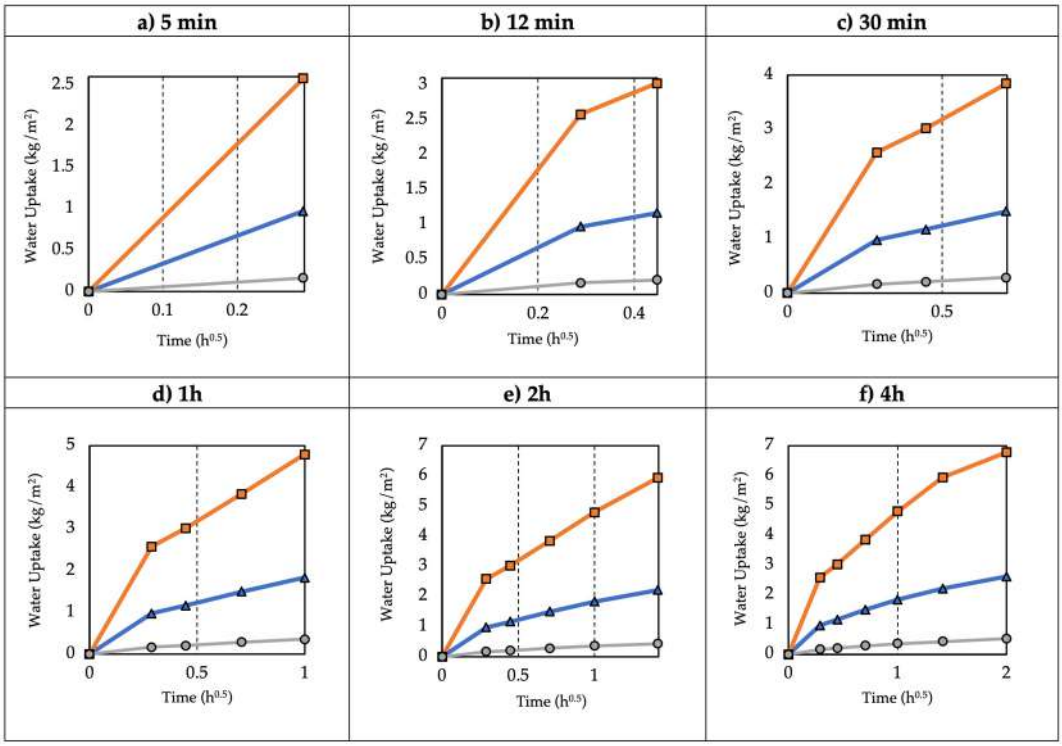

Fig. 14. IRA test results: Water uptake for (a) 5 min, (b) 12 min, (c) 30 min, (d) 1h, (e) 2h, and (f) 4h

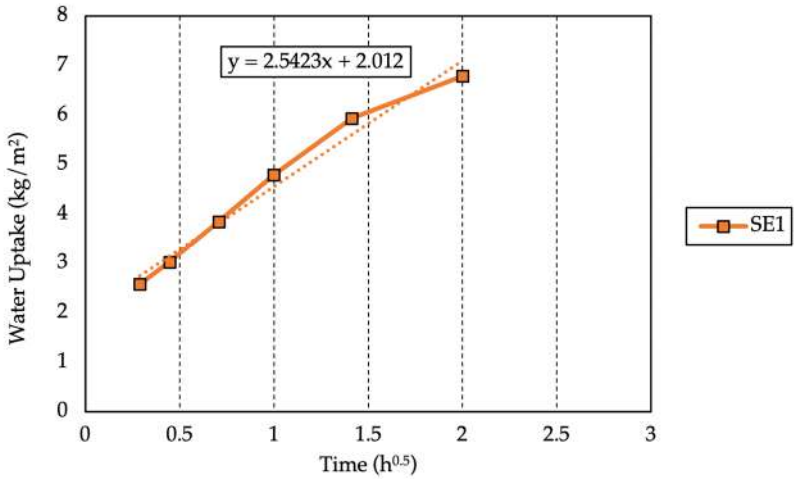

Fig. 15. Sorptivity coefficient (S) of SE1 derived from linear regression of water uptake

Table 4. Sorption coefficients at 5 minutes and 24 hours for SE2, SE1, and C45

Sorption coefficients		kg/(m²h^0.5)	kg/(m²min^0.5)	m/h^0.5	mm/min^0.5	Behavior
SE2	*5 min*	3.4	0.263	0.00324	0.419	*Linear*
	24 h	0.8	0.062	0.00081	0.105	*Non-Linear*
SE1	*5 min*	8.9	0.689	0.00883	1.140	*Linear*
	24 h	3	0.232	0.00142	0.184	*Linear*
C45	*5 min*	0.5	0.039	0.00277	0.053	*Linear*
	24 h	0.2	0.015	0.00067	0.018	*Non-Linear*

3.4. Immersion Test

Specimens used in the IRA test were subjected to full immersion for 7 days. Mass gain was monitored daily and normalized using √t to analyze non-linear absorption behavior. SE1 reached saturation rapidly, with over 8% water uptake. SE2 and C45 absorbed more slowly (**Fig. 16**). As shown in the following, these data turn out to be crucial to calibrate the FE model by Dp_{corr} (see **Eq. (3)**).

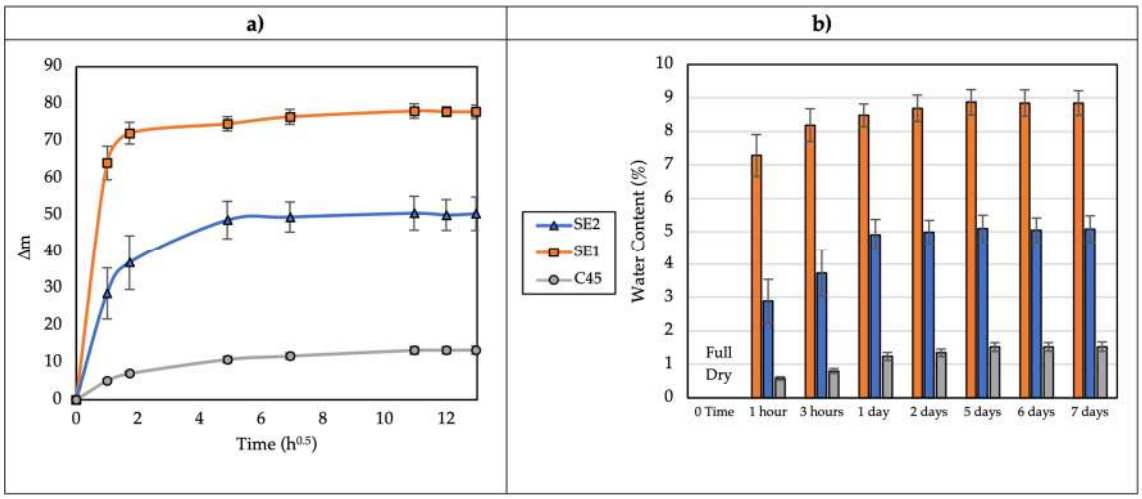

Fig. 16. (a) Immersion absorption pattern, while (b) shows water content (%) over time, reflecting saturation kinetics among the three materials

3.5. Water Permeability Test

Water permeability was assessed under two pressure regimes. The 500 kPa test resulted in structural failure of SE1 and SE2; therefore, a reduced 200 kPa test was applied successfully for 72 hours. C45 showed the lowest permeability, while SE1 displayed the highest. Using test data, saturated and unsaturated permeability, K (m/s) and K_s (m/s), intrinsic permeability, κ (m^2), and diffusivity, D (m^2/s), coefficients were calculated according to **[15,52,56]**, see **Table 5**.

Table 5. Saturated and unsaturated permeability, diffusivity, and intrinsic permeability for SE1, SE2, and C45; ϕ and l1 stand for porosity and waterfront rising over the test of time, respectively

	l1 (m)	ϕ	Water viscosity (Pa s)	P (kPa)	Time (s)	Ks (m/s)	K (m/s)	D (m^2/s)	κ (m^2)
SE2	0.084	0.17	0.001002	20.38	172800	2.026e-09	1.833e-09	1.300e-11	1.965e-16
SE1	0.137	0.18	0.001002	20.38	172800	3.499e-09	3.166e-09	2.010e-10	3.373e-16
C45	0.0145	0.15	0.001002	20.38	172800	3.086e-10	2.793e-09	1.135e-12	1.972e-17

3.6. Analytical Modeling

The simplified model was applied, and the relationship between the sorption coefficient S and degree of saturation is inferred for each material involved. IRA data were used to calibrate this model (see **Section 3.3**), which successfully predicted material behaviour across mixtures. As shown in **Fig. 17**, the curves for SE1, SE2, and C45 matched experimental absorption capacities. According to **Eq (1)** and **Eq (2)**, $\Lambda = 0$ corresponds to Si = 1…n(Λ) = Si = 0, representing the maximum absorption capacity under initial full-dry conditions. Then, the degree of saturation is calculated by taking the positive solution of the quadratic equation. On the other hand, when $\Lambda = 1$, Si = 1…n(Λ) = 0, and this indicates that the material has reached full saturation and no further absorption occurs. Using the model, the initial capillary absorption ratio for any degree of saturation Λ can be straightforwardly calculated from the absorption ratio measured under fully dry conditions.

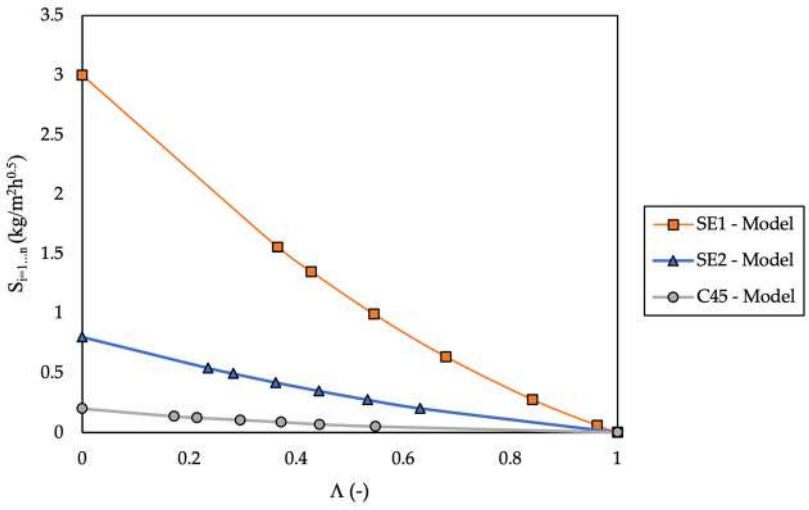

Fig. 17. Polynomial model fitting: relationship between absorption and saturation degree for SE1, SE2, and C45

3.7. FE modeling and calibration

To allow comparison with IRA experimental data, the simulation covered a time interval of two hours, after which the waterfront high was marked and compared with the experimental results. However, the authors observed a significant discrepancy in the permeability values obtained using the simplified Ergun theory among different materials. For instance, C45, while being the highest-performing material in the present, also has the largest average particle diameter D_P, as it includes aggregates ranging from 16 to 32 mm size. Consequently, the average diameter was determined to be 0.8 cm. When applying Ergun theory, the resulting permeability was found to be over four orders of magnitude higher than expected, leading to the conclusion that this value is fundamentally incorrect and not representative of the real material behavior in absorption. The permeability issue was addressed to *Felipe Montes et al.* **[65]**, who established correlations between the Ergun equation and the Reynolds number. By making empirical assumptions about particle diameters, he determined that the optimal way to account for the true density of concrete is to reduce the average particle size by an order of magnitude — from the typical value of 1 cm for ordinary concrete to 0.1 cm. When this value was adopted as input data for numerical analyses, as shown in **Table 6**, the simulation matches well the experimental data. **Fig. 18** confirms the waterfront rise and the proper match between the experimental data and FE simulation for C45.

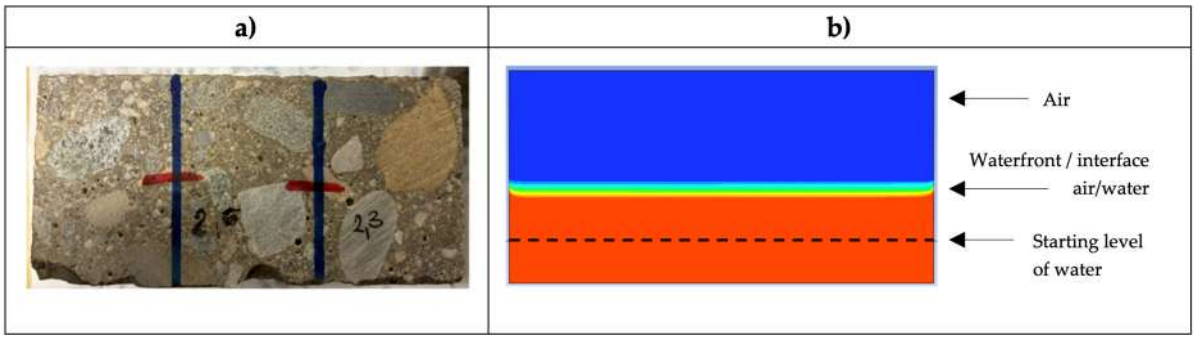

Fig. 18. (a) Experimental waterfront *vs* (b) FE simulation rising for C45: the red portion indicates the water, starting from 1 cm high, the blue region denotes the air that leaves the sample, and the green region represents the interface

The triple-axis graph (**Fig. 19**) presented below shows that selecting an average diameter of 0.1 cm for C45 is appropriate when considering the actual intrinsic permeability on the left-side y-axis. However, this is not the case for the permeability of a packed bed predicted through the FE modeling on the right-side y-axis. Notably, this low permeability results in a calculated value that is even negative, which would theoretically suggest the use of a negative diameter. This underscores the critical importance of

accurately representing the average particle size in modeling the porous media. Based on experimental data and material cohesion properties such as porosity and water capacity, two reference diameters such as 0.2 cm for SE2 and 0.5 cm for SE1 (**Table 6**) were both selected to establish a linear relationship between the three possible diameters and the values of permeabilities, and the equation has been extrapolated. On the left-side y-axis, the grey point stands for the actual intrinsic permeability — expressed in m^2 — of C45, while the blue and orange ones are for SE2 and SE1, respectively. However, the choice of 0.2 cm for SE2 reveals a significant deviation between the actual intrinsic permeability and the chosen diameter. In contrast, the 0.5 cm diameter for SE1 proves to be representative, as that for C45. These findings indicate the necessity of developing an exponential analytical relationship to correlate established values in the Literature with analogous values for other porous media, see **Eq. (3)**. Thus, an exponential correlation is proposed, accounting for the maximum water content of each material (expressed in percentage) in compliance with the reference concrete with known modified average diameter.

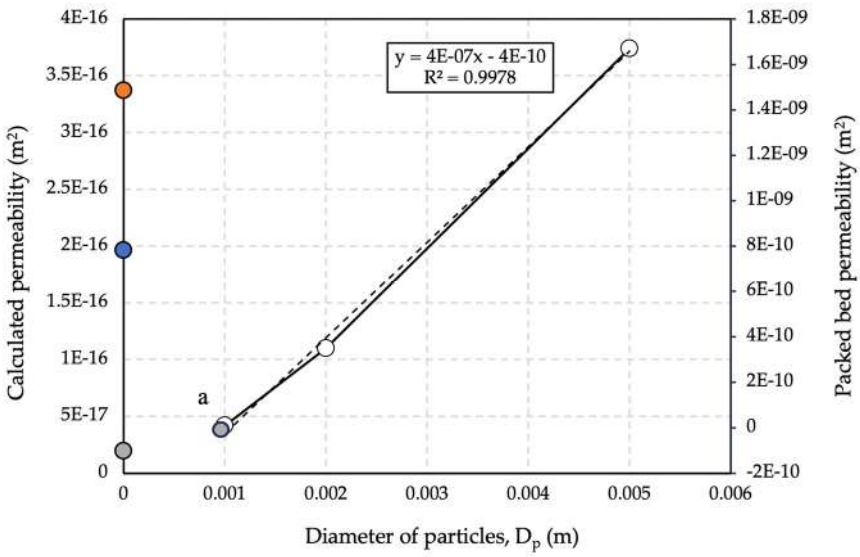

Fig. 19. C45 matching experimental data by confirming D_P = 0.1 cm. Point *a* represents the position of packed bed permeability compared to the experimentally calculated one by 0.1 cm D_P

$$Dp_{corr} = Dp_{real}\left(\frac{W_{a,porousmedia}}{W_{a,concrete}}\right)^{\alpha} \quad \text{with } \alpha \in [0.5 - 1] \tag{3}$$

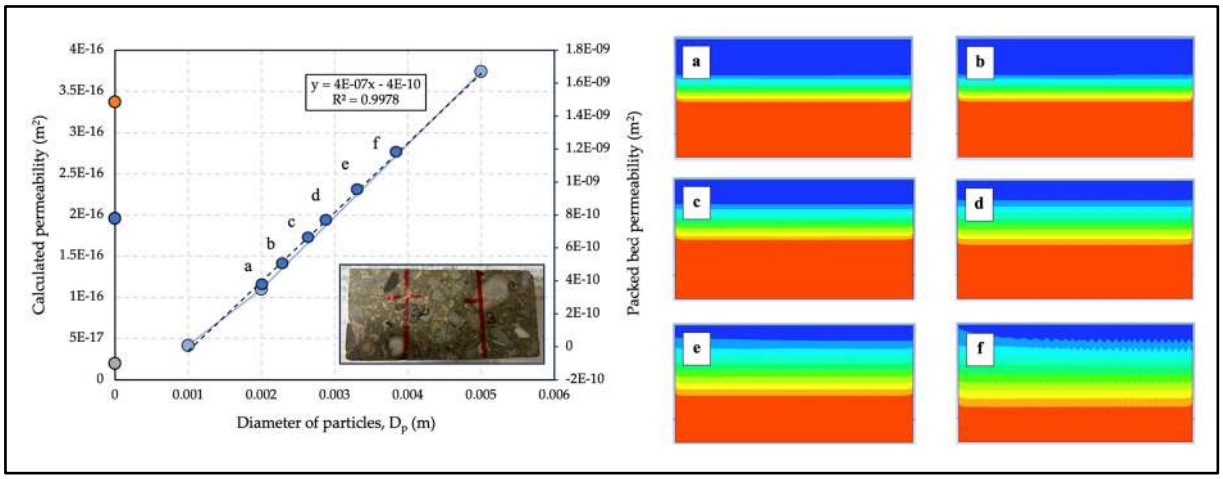

Fig. 20. FE predictions and experimental data in terms of permeability for SE2 using corrected D_P. On the right: FE simulation of capillary rise as a function of the average particle size D_P: the red regions indicate water penetration into the sample, while blue regions denote the air leaving

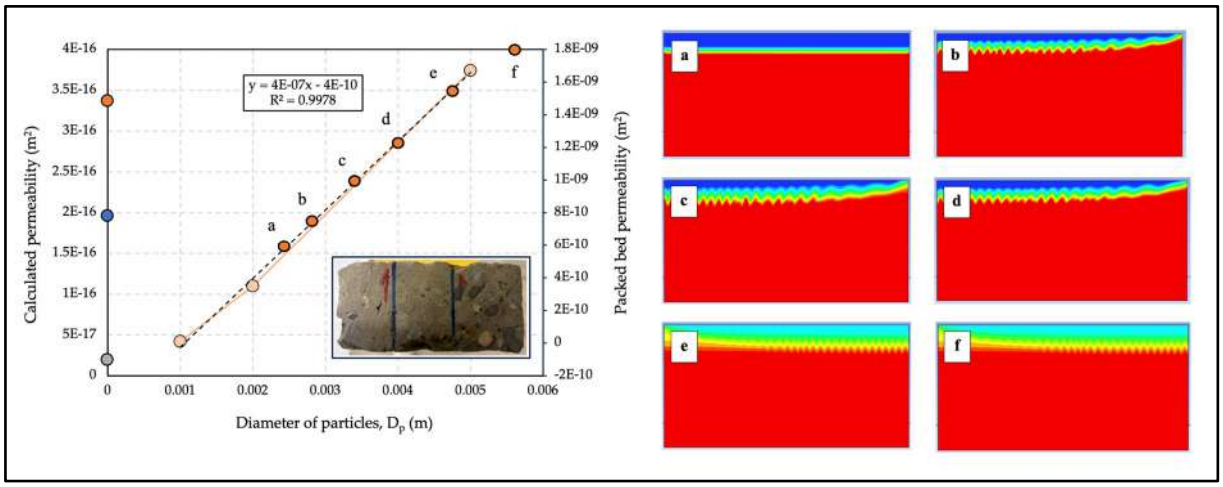

Fig. 21. FE predictions and experimental data in terms of permeability for SE1 using corrected D_P. On the right: FE simulation of capillary rise as a function of the average particle size D_P: the red regions indicate water penetration into the sample, while blue regions denote the air leaving

Table 6. Resuming table of FE modeling by Ergun's theory

	D_P (m)	Porosity (-)	a, constant (-)	Constant of Forchheimer, k1 (m)	k/k_{model} (m^2)	α (m^2)	C2 (1/m)
SE2	0.002	0.1784	150	7.898E-06	2.243E-10	-	-
SE1	0.005	0.1877	150	2.326E-05	1.67035E-09	-	-
C45	0.001	0.1037	-	7.10959E-07	9.25419E-12	9.25419E-12	126614.6426

By varying both the ratio of water content relative to that of C45, taken as reference, and the corresponding α-values, a wide range of average particle diameters was generated for both mixtures. For SE2, the fictitiously assigned value aligns well with the experimental results, indicating its suitability. Additionally, as the average diameter increases, the waterfront propagation increases proportionally, as permeability does. However, all results remain within acceptable tolerance limits (**Fig. 20)**. The same reasoning applies to SE1 (**Fig. 21**). Summarily, the diameters that best represent SE2 were found to range from 0.18 to 0.33 cm, while for SE1, they ranged from 0.24 to 0.48 cm.

4. Discussion

4.1. Analytical and FE modelling

The simplified analytical model successfully captured the absorption behavior of SE1-2 and C45, using polynomial expressions based on the degree of saturation. This approach offers a fast and effective method to predict water uptake from IRA data without requiring full-scale simulations. While more complex, FE modeling proved to be a powerful tool for validating and extrapolating experimental results. Starting the simulation with particle diameter (D_P) of 0.1 cm for C45 was crucial to interpolate the correct permeability values for SE1 and SE2. Moreover, calibrating D_P based on experimental fitting yielded more accurate representations of fluid flow in porous medium. The combined use of empirical testing and modeling has proven effective in assessing non-standard construction materials.

4.2. Durability Insights

The findings of this study confirm that water remains one of the most detrimental environmental agents impacting the durability of earth-based materials. Both capillary absorption and immersion tests revealed that Shot-Earth — particularly the SE1 mix — exhibits high water uptake under saturated conditions. While Shot-Earth offers excellent mechanical strength and early-age performance, its vulnerability to moisture exposure is a legitimate concern. However, this concern must be viewed in a broader architectural and historical context. Many traditional earthen materials—such as adobe and rammed earth—also exhibit high water sorptivity, yet have endured for centuries, often in demanding environmental conditions. Their resilience stems not from impermeability, but from careful design, detailing, and construction practices that adapt to the inherent properties of the material. In this regard, the present study provides a foundation for identifying where water-related durability challenges may emerge and how they can be addressed through thoughtful planning. The results also show that prolonged moisture exposure leads to a progressive loss of cohesion and mechanical integrity, particularly in SE1. In capillary-driven scenarios—such as rising damp—SE1's rapid and linear saturation behavior reflects its high affinity for moisture, likely due to its higher porosity and lower binder content as compared to SE2 and C45. These findings highlight the critical importance of moisture management when working with earthen materials, including the implementation of capillary breaks, breathable coatings, elevated foundations, and proper drainage. Importantly, Shot-Earth is a highly adaptable material system. Its dry application process allows for easy adjustment of the mix design, facilitating transitions between SE1 and SE2 as needed. Moreover, the same projection equipment and technique can be used to apply conventional concrete or shotcrete, offering exceptional construction flexibility. Owing to its high green strength, different segments of a wall can be constructed using tailored mix designs: for instance, a more water-resistant or cement-rich formulation can be applied at

the base, where exposure to rising damp is highest, while the level of stabilization can be gradually reduced in the upper sections where moisture exposure is minimal. This stratified construction strategy has long been employed across various materials and architectural traditions. A notable example is the project illustrated in **Fig. 22**, adapted in **[66]**, in which a rammed earth structural arch is supported by a solid stone base. Such layered configurations enable practitioners to optimize both performance and sustainability without altering the overall construction method.

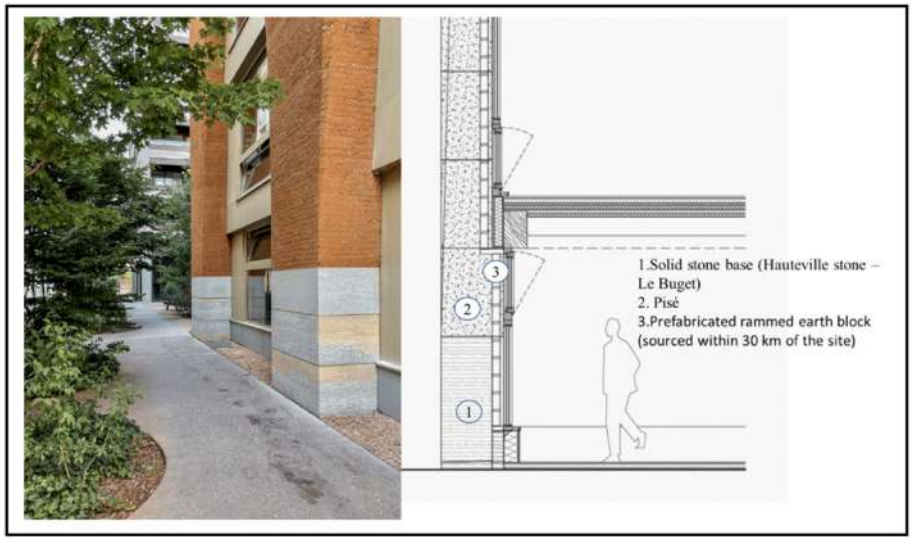

Fig. 22. Lyon, Confluence II (France), stratified construction by using pisé and rammed earth blocks **[66]**

5. Conclusion

This study evaluated the durability and water absorption behavior of Shot-Earth — a sustainable, soil-based construction material — through comprehensive experimental testing and numerical modeling. Two Shot-Earth mixtures (SE1 and SE2) were assessed and compared with conventional concrete (C45) under capillary rise, full immersion, and pressurized water exposure. The key conclusions are as follows:

- Moisture is the critical durability factor for earthen materials. A correlation exists between compressive strength, density, and water absorption capacity: SE1 absorbed 8.85% (7.72 MPa), SE2 improved to 5.09% (20.30 MPa), yet both remain above C45, which absorbed only 1.52% (45.5 MPa). Denser, stronger matrices are more resistant to water absorption. SE2 marks progress over SE1 but still requires stabilization to achieve concrete-level durability.
- Permeability remains a limitation. Shot-Earth permeability (3.373×10^{-16} m² for SE1 and 1.965×10^{-16} m² for SE2) is an order of magnitude higher than that of OPC concrete (1.972×10^{-17} m²). This may restrict its use in moisture-intensive environments unless appropriate protective measures — such as base detailing, breathable coatings, or elevated foundations — are applied.

- The absorption capacity measured by the sorption coefficient S ($kg/m^2h^{0.5}$) can be analytically evaluated using **Eq. (1)** and **Eq. (2)** at any time and at any degree of saturation once the initial dry mass and the final fully saturated mass are known.
- Using ordinary Portland cement concrete C45 as reference (1.52% maximum water content, 0.001 m particle size), the FE model shown that numerical simulations are a valid tool to predict water transport in Shot-Earth. The computational procedure requires the adoption of a proper reference diameter assessed through a best-fit scheme of the particle sizes through **Eq. (3**). The corrected average particle size D_p turns out to be 0.002 m for SE2 and 0.005 m for SE1, while porosity had limited influence. The proposed approach can be extended easily to other cementitious materials.

Beyond durability, Shot-Earth demonstrates substantial environmental advantages. Excavated soil accounts and aggregate have the same volume in all mixes studied, while binder content is reduced by more than 20% in SE2 and 60% in SE1 compared to OPC concrete — enabling both structural and non-structural applications. Moreover, in many cases (e.g., walls), only localized zones such as wall bases require enhanced water resistance and thus heavier stabilization. The Shot-Earth spraying process allows binder content or type to be quickly adapted *in situ* without halting construction. Its dry application also greatly facilitates the incorporation of CO_2-negative additives, further reinforcing its potential as a climate-positive construction technology. At the same time, further research remains essential. While this study focused on water-related degradation, other durability factors — such as freeze–thaw cycles, wet–dry cycles, salt crystallization, biological growth, and combined hygrothermal effects, still require systematic investigation. Mesoscale approaches, such as time of wetness (TOW) experiments, are carried out throughout the evaluation to the surface resistivity, rising damp, wet–dry processes, carbonation, and real-aging conditions. Preliminary investigations indicate that Shot-Earth's response to these stressors is highly dependent on mix design and binder content, but standardized test methods are often unsuitable for earthen composites. Developing adapted durability protocols therefore represents a challenging next step to assess the long-term performance and to position earthen composites such as Shot-Earth within building standards. Expanding the modeling framework to account for coupled phenomena (e.g., hygrothermal transport, gas permeability) would also broaden its predictive value. In conclusion, Shot-Earth and more broadly earthen materials is not yet a universal substitute for concrete in durability-critical applications. However, its environmental benefits, adaptability, and promising mechanical performance — combined with targeted protective detailing and further research on durability mechanisms — position it as a credible candidate for climate-positive construction technologies.

Acknowledgments

Financial support from the HES-SO in the framework of the projects « NextEarthBuild – Une nouvelle génération d'éco-construction en terre d'excavation recycle – n° 98528 » and « EcoAbri – Construction d'un abri témoin en terre d'excavation et autres matériaux écologiques et indigènes en vue de la réalisation ultérieure d'un espace de rangement non chauffé – n° 108222 » is gratefully acknowledged. Financial support from Innosuisse in the framework of the Project FieldEarth: a sustainable excavated-soil based building material – n° 52127.1 IP-EE » is gratefully acknowledged as well. AMT gratefully acknowledges the financial support of the MUR through the research grant PRIN 2022 (prot. 2022Y2RHHT; CUP E53D23003900006) and project FISA-2022-00183 "EARTH-TECH: Implementation of new Shot-Earth technology in the construction industry (CUP: E93C24000250001)".

References

[1] Gnanli Landrou, Ouellet-Plamondon, Brumaud, Coralie, Habert, Development of a Self-Compacted Clay based Concrete, rheological, mechanical and environmental investigations, (2014). https://doi.org/10.13140/2.1.1054.2401.

[2] A. Azil, K. Touati, N. Sebaibi, M. Le Guern, F. Streiff, S. Goodhew, M. Gomina, M. Boutouil, Monitoring of drying kinetics evolution and hygrothermal properties of new earth-based materials using climatic chamber simulation, Case Studies in Construction Materials 18 (2023) e01798. https://doi.org/10.1016/j.cscm.2022.e01798.

[3] «History of raw earth architecture» Available: https://www.architectural-review.com/essays/inhabiting-the-earth-a-new-history-of-raw-earth-architecture.

[4] Dethier J. Des architectures de terre: ou, l'avenir d'une tradition millénaire. Paris: Éditions du Centre Pompidou, 1986.

[5] Walker, P., & Standards Australia. HB 195: The Australian Earth Building Handbook. Standards Australia International, Sydney, 2002.

[6] M. Doğruyol, A. Gönül, O. Tunçel, B. Altun, A. Yılmaz, M. Durmaz, F. Hansu, Integrated assessment of mechanical, microstructural, and thermal behaviour of a fly ash-stabilized earthen building material, Journal of Building Engineering 113 (2025) 113871. https://doi.org/10.1016/j.jobe.2025.113871.

[7] T. Colinart, T. Vinceslas, H. Lenormand, A.H.D. Menibus, E. Hamard, T. Lecompte, Hygrothermal properties of light-earth building materials, Journal of Building Engineering 29 (2020) 101134. https://doi.org/10.1016/j.jobe.2019.101134.

[8] M. Bacciocchi, V. Savino, L. Lanzoni, A.M. Tarantino, M. Viviani, Multi-phase homogenization procedure for estimating the mechanical properties of shot-earth materials, Composite Structures 295 (2022) 115799. https://doi.org/10.1016/j.compstruct.2022.115799.

[9] A. Curto, L. Lanzoni, A.M. Tarantino, M. Viviani, Shot-earth for sustainable constructions, Construction and Building Materials 239 (2020) 117775. https://doi.org/10.1016/j.conbuildmat.2019.117775.

[10] S. Vantadori, A. Żak, Ł. Sadowski, C. Ronchei, D. Scorza, A. Zanichelli, M. Viviani, Microstructural, chemical and physical characterisation of the Shot-Earth 772, Construction and Building Materials 341 (2022) 127766. https://doi.org/10.1016/j.conbuildmat.2022.127766.

[11] M. Franciosi, V. Savino, L. Lanzoni, A.M. Tarantino, M. Viviani, Changing the approach to sustainable constructions: An adaptive mix-design calibration process for earth composite materials, Composite Structures 319 (2023) 117143. https://doi.org/10.1016/j.compstruct.2023.117143.

[12] A.M. Tarantino, F. Cotana, M. Viviani, eds., Shot-Earth for an Eco-friendly and Human-Comfortable Construction Industry, Springer Nature Switzerland, Cham, 2023. https://doi.org/10.1007/978-3-031-23507-8.

[13] M. Franciosi, V. Savino, L. Lanzoni, A.M. Tarantino, M. Viviani, Experimental investigation of Catalan vault structures based on earthen materials, Case Studies in Construction Materials 21 (2024) e03565. https://doi.org/10.1016/j.cscm.2024.e03565.

[14] M. Franciosi, V. Savino, L. Lanzoni, A.M. Tarantino, M. Viviani, Structural design of reinforced earthcrete (ReC) beams, Engineering Structures 306 (2024) 117739. https://doi.org/10.1016/j.engstruct.2024.117739.

[15] Benefits of dry/wet spraying concrete, (2015). https://mapleconcretepumping.ca/benefits-of-dry-mix-wet-mix-spraying-concrete/.

[16] L. Kong, B. Ma, Evaluation of environmental impact of construction waste disposal based on fuzzy set analysis, Environmental Technology & Innovation 19 (2020) 100877. https://doi.org/10.1016/j.eti.2020.100877.

[17] J. Cristóbal, G. Foster, D. Caro, F. Yunta, S. Manfredi, D. Tonini, Management of excavated soil and dredging spoil waste from construction and demolition within the EU: Practices, impacts and perspectives, Science of The Total Environment 944 (2024) 173859. https://doi.org/10.1016/j.scitotenv.2024.173859.

[18] M. Franciosi, V. Savino, L. Lanzoni, A.M. Tarantino, M. Viviani, Long-Term Creep Behavior of New Earth Composite Materials, J. Mater. Civ. Eng. 37 (2025) 04025131. https://doi.org/10.1061/JMCEE7.MTENG-17216.

[19] V. Savino, M. Franciosi, M. Viviani, Engineering and analyses of a novel Catalan vault, Engineering Failure Analysis 143 (2023) 106841. https://doi.org/10.1016/j.engfailanal.2022.106841.

[20] L.B. Traoré, C. Ouellet-Plamondon, A. Fabbri, F. McGregor, F. Rojat, Experimental assessment of freezing-thawing resistance of rammed earth buildings, Construction and Building Materials 274 (2021) 121917. https://doi.org/10.1016/j.conbuildmat.2020.121917.

[21] S. Chehade, N. Dujardin, D. Giovannacci, A. Boudenne, Experimental and numerical evaluation of heat and mass transfer of a compressed raw earth block wall, Case Studies in Construction Materials 22 (2025) e04793. https://doi.org/10.1016/j.cscm.2025.e04793.

[22] P. Wiehle, M. Härder, C. Strangfeld, Quantification of moisture content in earth block masonry under natural climatic conditions, Construction and Building Materials 459 (2025) 139513. https://doi.org/10.1016/j.conbuildmat.2024.139513.

[23] S. Rafraf, L. Guellouz, H. Guiras, R. Bouhlila, Quantification of hysteresis effects on a soil subjected to drying and wetting cycles, International Agrophysics 30 (2016) 493–499. https://doi.org/10.1515/intag-2016-0020.

[24] L. Barbieri, L. Lanzoni, R. Marchetti, S. Iotti, A.M. Tarantino, I. Lancellotti, Shot-Earth as Sustainable Construction Material: Chemical Aspects and Physical Performance, Sustainability 16 (2024) 2444. https://doi.org/10.3390/su16062444.

[25] Y.-W. Liu, T. Yen, T.-H. Hsu, Abrasion erosion of concrete by water-borne sand, Cement and Concrete Research 36 (2006) 1814–1820. https://doi.org/10.1016/j.cemconres.2005.03.018.

[26] M. Gasc-Barbier, V. Merrien-Soukatchoff, Effect of Freezing-Thawing Cycles on the Elastic Waves' Properties of Rocks, Geosciences 12 (2022) 103. https://doi.org/10.3390/geosciences12030103.

[27] M. S. Jones, Building Research Association of New Zealand (BRANZ), Judgeford, Effects of UV Radiation on Building Materials (2002).

[28] RILEM Technical Committee 200-HTC, Recommendation of RILEM TC 200-HTC: mechanical concrete properties at high temperatures—modelling and applications: Part 1: Introduction—General presentation, Mater Struct 40 (2007) 841–853. https://doi.org/10.1617/s11527-007-9285-2.

[29] F. Gomes, R. Brière, A. Feraille, G. Habert, S. Lasvaux, C. Tessier, Adaptation of environmental data to national and sectorial context: application for reinforcing steel sold on the French market, Int J Life Cycle Assess 18 (2013) 926–938. https://doi.org/10.1007/s11367-013-0558-4.

[30] Kindermans M (2017) Sevran recycle ses terres. Echos 1, 2017.

[31] A. Yousaf, S.A. Khan, M. Koç, Material, process, and design optimization of local earthen soil reinforced with natural fiber waste and nanoclay for 3DP of functional structures, Journal of Building Engineering 111 (2025) 113502. https://doi.org/10.1016/j.jobe.2025.113502.

[32] L. Casnedi, M. Cappai, A. Cincotti, F. Delogu, G. Pia, Porosity effects on water vapour permeability in earthen materials: Experimental evidence and modelling description, Journal of Building Engineering 27 (2020) 100987. https://doi.org/10.1016/j.jobe.2019.100987.

[33] Hammond AA. Prolongation de la dureé de vie des constructions en terre sous les tropiques. CDU 69.031973;213:167-97.

[34] D. Seyferth, The Rise and Fall of Tetraethyllead. 2., Organometallics 22 (2003) 5154–5178. https://doi.org/10.1021/om030621b.

[35] T. Midgley, Tetraethyl Lead Poison Hazards., Ind. Eng. Chem. 17 (1925) 827–828. https://doi.org/10.1021/ie50188a020.

[36] W. Nawaz, H. Bashir, Managing the unintended consequences of radical sustainability innovations: The case of catastrophic failure of leaded gasoline industry, Journal of Cleaner Production 375 (2022) 134175. https://doi.org/10.1016/j.jclepro.2022.134175.

[37] A. Manan, Z. Pu, M.M. Sabri, W. Alattyih, J. Ahmad, A. Alzlfawi, Environmental and human health impact of recycle concrete powder: an emergy-based LCA approach, Front. Environ. Sci. 12 (2025) 1505312. https://doi.org/10.3389/fenvs.2024.1505312.

[38] M.B. Subhani, A. Khitab, Carbon footprint reduction in mid-rise buildings: analysis, design, and LCA-based evaluation of alternate steel slag aggregates in concrete, Discov Civ Eng 2 (2025) 119. https://doi.org/10.1007/s44290-025-00276-y.

[39] SIA – Société Suisse des Ingénieurs et des Architectes. (2023). SIA 390/1: La voie du climat – Bilan des gaz à effet de serre et de l'énergie des bâtiments [Climate path – Partial greenhouse gas and energy balance of buildings]. Zurich: SIA.

[40] UNI EN 1936:2006 - Test methods for natural stones - Determination of real and apparent density and total and open porosity, 2006.

[41] ASTM C642-97 - Standard Test Method for Density, Absorption, and Voids in Hardened Concrete, 1997.

[42] EN 12390-19, Testing hardened concrete – Part 3: Compressive strength of test specimens, 2019.

[43] EN 13412:2006, Products and system for the protection and repair of concrete structures – Test methods – Determination of modulus of elasticity in compression, 2006.

[44] ASTM C469/C469M-14, Standard Test Method for Static Modulus of Elasticity and Poisson's Ratio of Concrete in Compression, 2014.

[45] D. Nicola, Profex and BGMN: Open-source software for phase analysis by X-ray diffraction, Front. Bioeng. Biotechnol. 4 (2016). https://doi.org/10.3389/conf.FBIOE.2016.01.02281.

[46] R.V. Balendran, H.W. Pang, H.X. Wen, Use of scanning electron microscopy in concrete studies, Structural Survey 16 (1998) 146–153. https://doi.org/10.1108/02630809810232718.

[47] S.S. Bangaru, C. Wang, X. Zhou, M. Hassan, Scanning electron microscopy (SEM) image segmentation for microstructure analysis of concrete using U-net convolutional neural network, Automation in Construction 144 (2022) 104602. https://doi.org/10.1016/j.autcon.2022.104602.

[48] S. Diamond, J. Huang, The ITZ in concrete – a different view based on image analysis and SEM observations, Cement and Concrete Composites 23 (2001) 179–188. https://doi.org/10.1016/S0958-9465(00)00065-2.

[49] L.R.C. Tavares, J.F.T. Junior, L.M. Costa, A.C. Da Silva Bezerra, P.R. Cetlin, M.T.P. Aguilar, Influence of quartz powder and silica fume on the performance of Portland cement, Sci Rep 10 (2020) 21461. https://doi.org/10.1038/s41598-020-78567-w.

[50] BS EN 933-1 - Tests for geometrical properties of aggregates Part 1: Determination of particle size distribution — Sieving method, 2012.

[51] SN 670 816a - Swiss Standard for Raw Earth Construction: Technical Specifications and Test Methodologies.

[52] BS EN 13057:2002 - Products and systems for the protection and repair of concrete structures. Test methods. Determination of resistance of capillary absorption, 2002.

[53] AS/NZS 4456.17:2003 - Masonry Units, Segmental Pavers and Flags-Methods of Test - Determining Initial Rate of Absorption (Suction), 2003.

[54] DIN 1048-5, 1991 Edition, June 1991 - Testing concrete; testing of hardened concrete (specimens prepared in mould), 1991.

[55] ASTM D3967-16 - Standard Test Method for Splitting Tensile Strength of Intact Rock Core Specimens, 2016.

[56] BS EN 12390-8 - Testing Hardened Concrete Part 8: Depth of Penetration of Water Under Pressure, 2019.

[57] R.D. Barree, M.W. Conway, Beyond Beta Factors: A Complete Model for Darcy, Forchheimer, and Trans-Forchheimer Flow in Porous Media, in: SPE Annual Technical Conference and Exhibition, SPE, Houston, Texas, 2004. https://doi.org/10.2118/89325-ms.

[58] N. Dukhan, Ö. Bağcı, M. Özdemir, Experimental flow in various porous media and reconciliation of Forchheimer and Ergun relations, Experimental Thermal and Fluid Science 57 (2014) 425–433. https://doi.org/10.1016/j.expthermflusci.2014.06.011.

[59] Forchheimer Porous-media Flow Models - Numerical Investigation and Comparison with Experimental Data, Vishal Jambhekar, Thesis of Master.

[60] H. Ma, W. Xu, Y. Li, Random aggregate model for mesoscopic structures and mechanical analysis of fully-graded concrete, Computers & Structures 177 (2016) 103–113. https://doi.org/10.1016/j.compstruc.2016.09.005.

[61] L. Yang, G. Liu, D. Gao, C. Zhang, Experimental study on water absorption of unsaturated concrete: w/c ratio, coarse aggregate and saturation degree, Construction and Building Materials 272 (2021) 121945. https://doi.org/10.1016/j.conbuildmat.2020.121945.

[62] X. Li, S. Chen, Q. Xu, Y. Xu, Modeling the three-dimensional unsaturated water transport in concrete at the mesoscale, Computers & Structures 190 (2017) 61–74. https://doi.org/10.1016/j.compstruc.2017.05.005.

[63] C. He, E. Makovicky, B. Osback, Thermal stability and pozzolanic activity of calcined kaolin, Applied Clay Science 9 (1994) 165–187. https://doi.org/10.1016/0169-1317(94)90018-3.

[64] M. Hall, Y. Djerbib, Moisture ingress in rammed earth: Part 1—the effect of soil particle-size distribution on the rate of capillary suction, Construction and Building Materials 18 (2004) 269–280. https://doi.org/10.1016/j.conbuildmat.2003.11.002.

[65] F. Montes, L. Haselbach, Measuring Hydraulic Conductivity in Pervious Concrete, Environmental Engineering Science 23 (2006) 960–969. https://doi.org/10.1089/ees.2006.23.960.

[66] Joud Beaudoin Architectes. "Îlot mixte B2, Lyon Confluence II." Joud Beaudoin Architectes, 2021.